COMMUNICATIONS PHYSICS

There are amendments to this paper

ARTICLE

https://doi.org/10.1038/s42005-018-0100-x OPEN

Joule overheating poisons the fractional ac Josephson effect in topological Josephson junctions

Kévin Le Calvez[1], Louis Veyrat[1], Frédéric Gay[1], Philippe Plaindoux[1], Clemens B. Winkelmann[1], Hervé Courtois[1] & Benjamin Sacépé[1]

Topological Josephson junctions designed on the surface of a 3D-topological insulator harbor Majorana bound states among a continuum of conventional Andreev bound states. The distinct feature of these Majorana bound states lies in the 4π-periodicity of their energy-phase relation that yields a fractional ac Josephson effect and a suppression of odd Shapiro steps under radio-frequency irradiation. Yet, recent experiments showed that a few, or only the first, odd Shapiro steps are missing, casting doubts on the interpretation. Here we show that Josephson junctions tailored on the large bandgap 3D-topological insulator Bi_2Se_3 exhibit a fractional ac Josephson effect acting on the first Shapiro step only. With a modified resistively shunted junction model, we demonstrate that the resilience of higher order odd Shapiro steps can be accounted for by thermal poisoning driven by Joule overheating. Furthermore, we uncover a residual supercurrent at the nodes between Shapiro lobes, which provides a direct and novel signature of the current carried by the Majorana bound states. Our findings showcase the crucial role of thermal effects in topological Josephson junctions and lend support to the Majorana origin of the partial suppression of odd Shapiro steps.

[1] Univ. Grenoble Alpes, CNRS, Grenoble INP, Institut Néel, 38000 Grenoble, France. Correspondence and requests for materials should be addressed to B.S. (email: benjamin.sacepe@neel.cnrs.fr)

Topological superconductivity engineered by coupling superconducting electrodes to topological states of matter has attracted considerable attention due to the prospect of manipulating Majorana states for topological quantum computing[1–3]. Intense experimental efforts have focused on spectroscopic signatures of Majorana bound states (MBSs) in various superconductivity-proximitized systems, including semiconducting nanowires[4–8], atomic chains[9,10] or islands[11] of magnetic atoms, and vortices at the surface of 3D-topological insulators (TIs)[12].

Another key approach to substantiate the very existence of MBS relies on the fractional AC Josephson effect[13–15] that develops in topological Josephson junctions[3,15]. Theory predicts that MBSs shall emerge in such junctions as a peculiar, spinless Andreev bound state (ABS). Contrary to the conventional ABSs whose energy level varies 2π-periodically with the phase difference ϕ between the junction electrodes, the MBS is 4π-periodic and crosses zero-energy for a phase π (see Fig. 1a), yielding a fractional AC Josephson effect at frequency $f_J/2 = eV/h$ (e is the electron charge, V the voltage drop across the junction and h the Planck constant), that is, half the Josephson frequency f_J[3,15].

Yet, revealing such a 4π-periodic contribution has proven challenging in dc transport experiments due to the presence of often prevailing, conventional ABSs[16–18]. Moreover, poisoning processes—stochastic parity-changes of the quasiparticle occupation number—may obscure the MBS contribution by limiting its lifetime[19,20]. Measurement schemes probing at time scales shorter than this lifetime are thus essential. The Shapiro effect comes forth with the combined advantages of a radio-frequency (f_{rf}) excitation of the phase that can be faster than the poisoning dynamics[15,21,22], and the ease of dc current-voltage (I-Vs) characteristics measurements.

The immediate consequence of the fractional AC Josephson effect is an unusual sequence of Shapiro voltage steps $\Delta V = \frac{hf_{rf}}{e}$ in the I-V characteristics, twice of that of conventional Shapiro steps $\left(\frac{hf_{rf}}{2e}\right)$[13,21–26], providing direct evidence for the MBS 4π-periodicity. First experiments performed on InSb nanowires[27], on strained HgTe 3D TI[28], and on $Bi_{1-x}Sb_x$[29] junctions however showed surprises in the sequences of Shapiro steps. In all these cases, only the $n = \pm 1$ steps were absent in a given range of radio-frequency (rf) power and frequency (n is the integer index of the Shapiro steps), an absence which was described as an (incomplete) signature of the fractional a.c. Josephson effect. More recent measurements on 2D HgTe quantum wells showed the absence of odd steps up to $n = 9$[30] and Josephson radiation at half the Josephson frequency[31], though without the demonstration of time-reversal symmetry breaking that is required to induce MBSs in quantum spin-Hall edge channels[15,32]. While the latter observations advocate more clearly for the existence of 4π-periodic Andreev modes, the fact that the fractional AC Josephson effect acts only on some odd Shapiro steps depending on the system remains unclear. Whether it provides a signature of the Majorana mode is a central question for identifying topological superconductivity in a variety of implementations.

In this work we report on the observation and understanding of the partial fractional AC Josephson effect in Josephson junctions designed on exfoliated flakes of the 3D-topological insulator Bi_2Se_3. Our devices exhibit an anomalous sequence of Shapiro steps with (only) the first step absent at low rf power and frequency. The 4π-periodic contribution to the supercurrent is directly identified as a residual supercurrent at the first node of the critical current when the rf power is increased. To shed light on our findings, we develop a two-channel resistively shunted

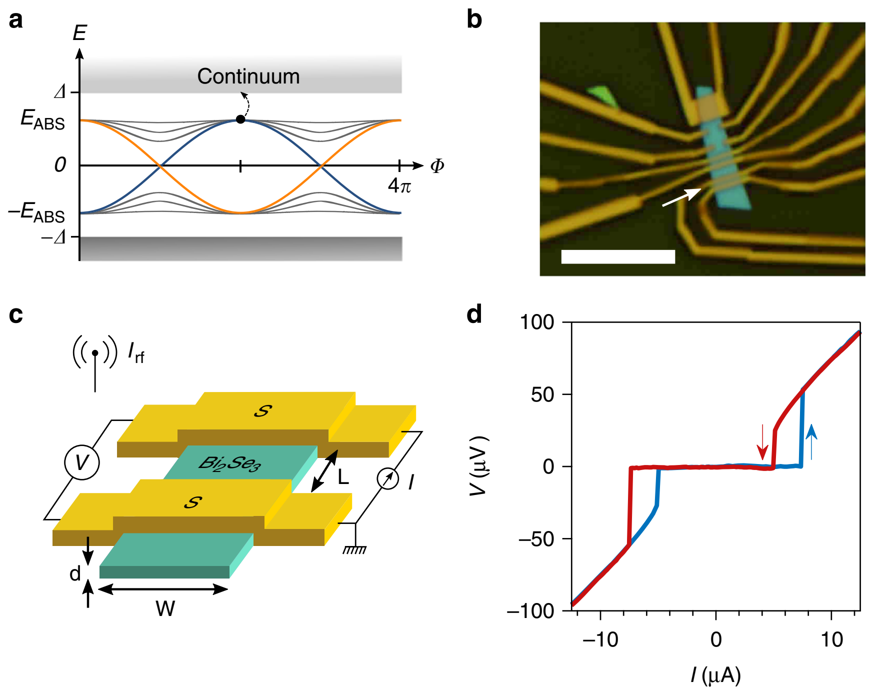

Fig. 1 Topological Josephson junction on Bi_2Se_3. **a** Energy-phase spectrum of the Andreev bound states for a topological Josephson junction at the surface of a 3D-topological insulator. 4π-periodic, spinless, Majorana bound states coexist with conventional 2π-periodic Andreev bound states (ABS). The maximum energy E_{ABS} is lower than the quasiparticle continuum at Δ in case of imperfect interface transparency or the presence of a magnetic barrier[3,15,43]. **b** Optical image of device. Scale bar is 9 µm. **c** Schematic of the Josephson junction geometry showing the superconducting electrodes (S) in orange that contact the top of the Bi_2Se_3 flake (in blue). **d** Current-voltage characteristic of the junction indicated by the arrow in **c**. Measurements were carried out at 0.05 K

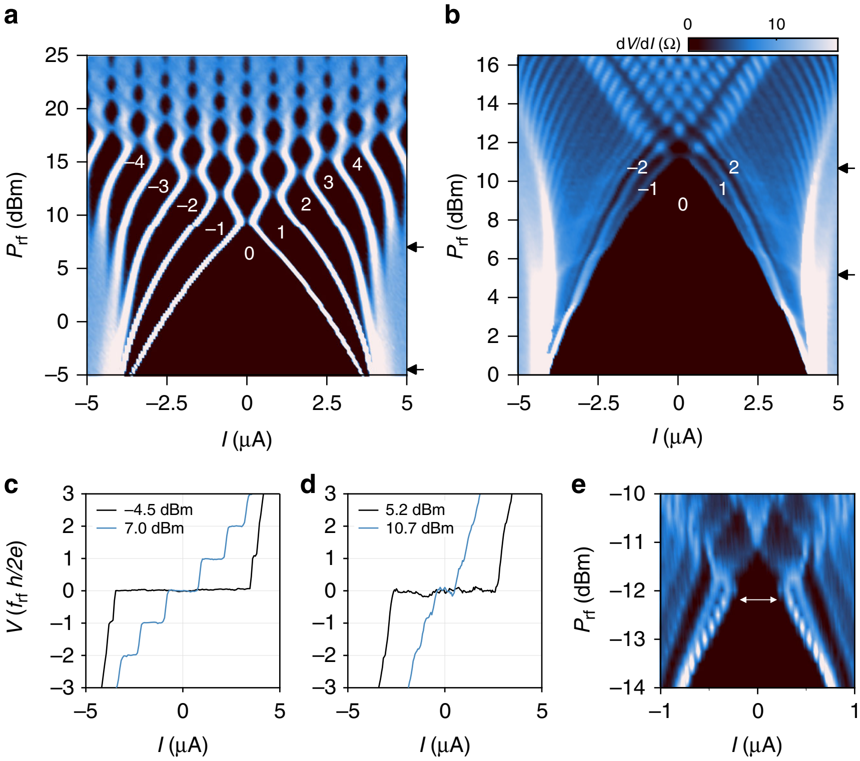

Fig. 2 Partial fractional AC Josephson effect. **a**, **b** Shapiro maps displaying the differential resistance dV/dI versus rf power P_{rf} applied to the antenna and dc current I measured at $f_{rf} = 3.5$ GHz in (**a**) and 1 GHz in (**b**). White numbers indicate the Shapiro steps index. **c**, **d** Voltage V in units of $f_{rf}h/2e$ versus I extracted from the Shapiro map in (**a**, **b**) respectively at two different P_{rf} values. The corresponding P_{rf} values are indicated by the black arrows in (**a**, **b**). **e** Shapiro map displaying dV/dI versus P_{rf} and I, measured at a different frequency $f_{rf} = 0.953$ GHz during a second cooling of the sample, and zoomed on the first resistive node. The white arrow indicates twice the residual supercurrent $\left(2\times I_0^{k=1}\right)$ at the first resistive node

junction (RSJ) model that includes the quasiparticle overheating induced by Joule effect[33–35], and a thermally activated poisoning of the MBS. We show that Joule overheating suppresses the parity lifetime of the MBS and thus terminates the 4π-periodic contribution to any higher index Shapiro steps, accounting for the observed suppression of the first Shapiro step only.

Results

Partial even-odd effect in Bi_2Se_3 Josephson junctions. Our samples are based on flakes of Bi_2Se_3 crystals exfoliated with the scotch tape technique. Figure 1b shows a 30 nm thick flake of Bi_2Se_3 contacted with multiple electrodes of vanadium enabling both magneto-transport and Josephson junction measurements on the same Bi_2Se_3 crystal (see Appendix for fabrication and measurement details). Analysis of Shubnikov-de-Haas oscillations and Hall effect enable identification of three electronic populations contributing to the sample conductance: Bulk states with a charge carrier density of 4.5×10^{19} cm^{-3}, and the top and bottom surface states with densities of 1×10^{12} and 4×10^{12} cm^{-2} respectively (see Supplementary Note 1). All three channels may thus carry supercurrent by proximity effect[36].

We focus here our discussion on the Josephson junction of length $L = 125$ nm and width $W = 2.25$ μm (see geometry in Fig. 1c) indicated by the white arrow in Fig. 1c. Below the superconducting transition temperature of the electrodes ($T_c = 5$ K), the proximity effect develops in the TI, leading to a dissipationless supercurrent in the I-Vs as shown in Fig. 1d (see Supplementary Note 2 for I-Vs at higher current bias showing an excess current due to Andreev reflections). The transition to the resistive state of the junction ($R = 7.5\ \Omega$) is hysteretic at 0.05 K with switching and retrapping currents of $I_{sw} = 7.3$ μA and $I_r = 5.0$ μA, respectively. Such a hysteresis is a common feature of most Josephson junctions made with metallic weak links and results from a quasiparticle overheating in the normal section of the junction[34]. As we will show below, the ensuing quasiparticle overheating is key for understanding the suppression of the $n = \pm1$ Shapiro steps only.

The dc response of the Josephson junction to an rf irradiation is shown in the Shapiro maps of Fig. 2a, b that display the color-coded differential resistance dV/dI versus rf power P_{rf} and dc current I. For an rf frequency of 3.5 GHz, Fig. 2a, well-defined Shapiro steps develop in the $I-V$ curves, two of which are shown in Fig. 2c, with voltage steps that match the standard value $V_n = \pm n\frac{hf_{rf}}{2e} = n\times7.2$ μV expected for a 2π-periodic current-phase relation. In the Shapiro map, the black areas indicate dV/d$I = 0$ and hence the position and amplitude of the Shapiro steps in the $P_{rf}-I$ plane. Two features standard for a usual Shapiro map are visible. First, on increasing P_{rf}, the critical current continuously decreases till nearly full suppression at $P_{rf} = 9$ dBm and then oscillates at higher P_{rf}. Second, the sequence of appearance of the Shapiro steps with P_{rf} is sorted by the Shapiro step index n, and, importantly, starts with the step $n = 1$.

The central experimental result of this work is displayed in Fig. 2b, where we show the rf response of the same junction at a lower frequency of 1 GHz. This Shapiro map exhibits distinct features that markedly differentiate it from the higher frequency map. On increasing P_{rf}, the first Shapiro step $n = 1$ sets in at high P_{rf} after the steps of higher index for both switching and retrapping currents. This anomaly, sometimes termed even-odd effect[21,22], results in the conspicuous absence of the first Shapiro step in I–Vs picked out at low $P_{\rm rf}$, while steps of higher indexes already appears, see Fig. 2d (similar results obtained on another sample are shown in Supplementary Note 3). Our findings match those recently obtained on InSb nanowires[27], strained HgTe 3D TI[28] and $Bi_{1-x}Sb_x$ alloy[29], which were interpreted as a signature of a 4π-periodic MBS contribution.

A second and new feature emerges at the first minimum of the critical current when the rf power is increased, i.e., at $P_{\rm rf} \simeq$ 10.7 dBm. Contrary to a conventional Shapiro map where a complete supercurrent suppression is expected at what can be called a resistive node, a small supercurrent $I_{\rm c} \sim 190$ nA remains. This appears clearly in the individual I-Vs of Fig. 2d, see for instance the blue curve there. Figure 2e displays a similar Shapiro map obtained at a slightly different $f_{\rm rf}$ in the low-frequency regime, but zoomed on the resistive node where the critical current is expected to vanish but does not. We shall see in the following that this residual supercurrent provides a direct signature of the presence of a 4π-periodic mode in the junction.

Determination of the coherent transport regimes. Capturing the ABS spectrum of a Josephson junction on 3D TIs remains difficult as several conduction channels, including bulk and surfaces, intervene. Should all channels carry supercurrent, the nature of charge carriers in them may lead to virtually different regimes of coherent transport that we assess in the following. For bulk carriers, a rough estimate of the mean-free path (see Supplementary Note 1) gives a Thouless energy $E_{\rm th} = \hbar D/L^2 \simeq$ 417 μeV, smaller than the superconducting gap of the vanadium electrodes $\Delta = 800$ μeV. This channel thus belong to the class of long diffusive Josephson junctions[37]. In contrast, for the topological surface states, the spin texture of the Dirac electrons stemming from the spin-momentum locking leads to a very strong scattering anisotropy which promotes forward scattering. As a result, the transport time $\tau_{\rm tr}$ is expected to be significantly enhanced with respect to the elastic scattering time $\tau_{\rm e}$, with ratio $\tau_{\rm tr}/\tau_{\rm e}$ up to 60 depending on the disorder source[38]. Recent experiments on Bi_2Se_3 flakes combining field effect mobility and quantum oscillations assessed a ratio $\tau_{\rm tr}/\tau_{\rm e} \gtrsim 8$[39]. Taking the latter value as a conservative estimate and the surface state elastic mean-free path $l_e \simeq 28$ nm of our sample (see Supplementary Note 1) leads to a transport length $l_{\rm tr} \gtrsim 225$ nm. These considerations suggest that surface transport is ballistic with, importantly, a non-zero probability for straight electronic trajectories impinging both electrodes. This is also consistent with signatures of ballistic transport over 300 nm evidenced in Bi_2Se_3 nanowires[40,41].

Consequently, we consider the topological surface state channel as ballistic. As such, the relevant energy scale for the ABSs is $\hbar v_{\rm F}/L = 2.8$ meV with $v_{\rm F} = 5.4 \times 10^5$ m/s the Fermi velocity[42]. It is greater than Δ, which shall lead to ABSs in the short ballistic limit. Theory then predicts that a 4π-periodic MBS exists, even in the case where the Fermi level is far from the Dirac point of the surface states, which is here the experimentally relevant regime[43]. This MBS corresponds to ballistic trajectories impinging perpendicularly the superconducting electrodes, all other incidence angles yielding conventional 2π-periodic ABSs[3,43].

Eventually, observability of the 4π-periodicity theoretically implies a strong constraint on the Andreev spectrum: The MBSs must be decoupled from the quasiparticle continuum at $\phi = 0$ and 2π to avoid direct transfer of quasiparticles into or from the continuum. Such a transition would indeed occur from the excited to the ground state every 2π, restoring an effective 2π-periodicity for the MBS. This detrimental effect can be remedied by adding a magnetic layer or magnetic field that break time-reversal symmetry, and thus open a gap between the MBS and the quasiparticle continuum[15,21,23,43,44], as sketched in Fig. 1a. In our samples, the vanadium that we use as superconducting electrodes is known to form magnetic dopants in Bi_2Se_3 and eventually a ferromagnetic phase at large concentration[45]. Given that a smooth ion milling of the Bi_2Se_3 surface is processed before vanadium deposition, favoring vanadium diffusion into the Bi_2Se_3 crystal, there is presumably a magnetic layer or local magnetic moments at the superconducting interface as well as magnetic moments on the oxidized vanadium side surfaces of the electrodes. This singular configuration is likely to break time-reversal symmetry on the scale of the junction, thus leading to the decoupling of the MBS from the continuum and to the ensuing observability of 4π-periodicity in our Shapiro maps.

Two-channel RSJ model. To understand our experimental findings, we consider a RSJ model comprising a pure Josephson junction in parallel with a shunt resistor R. In the usual scheme of a single Josephson channel with a critical current $I_{\rm c}$, the key parameter for the phase dynamics is the phase relaxation time $\tau_{\rm J} = \frac{\hbar}{2eRI_{\rm c}}$ which sets the typical time scale for the phase to adapt to a drive current change[33]. With a rf drive, the RSJ model thus acts on the phase as a low pass filter of cutoff frequency $1/\tau_{\rm J}$ (see Supplementary Note 4). The regime of visibility of Shapiro steps is thus defined by $f_{\rm rf}\tau_{\rm J} < 1$.

To phenomenologically capture the complex dynamics of a topological Josephson junction where a MBS lies within (a majority of) ABSs, we include two different Josephson junctions J1 and J2 in the RSJ model (see Fig. 3a)[24,26]. The first junction J1 stands for the conventional ABSs with a 2π-periodic current-phase relation, and the second one J2 represents the 4π-periodic MBSs.

Having both 2π and 4π-periodic contributions in the total supercurrent $I_{\rm s}(\phi) = I_{\rm c}^{2\pi}\sin(\phi) + I_{\rm c}^{4\pi}\sin(\phi/2)$ drastically changes the Shapiro steps sequence. The dynamics is now ruled by two different phase relaxation times $\tau_{\rm J}^{2\pi} = \frac{\hbar}{2eRI_{\rm c}^{2\pi}}$ and $\tau_{\rm J}^{4\pi} = \frac{\hbar}{eRI_{\rm c}^{4\pi}}$ set by the respective critical current amplitudes $I_{\rm c}^{2\pi}$ and $I_{\rm c}^{4\pi}$. Consequently, the 4π-periodic contribution will impact the junction dynamics only for drive frequencies $f_{\rm rf} < 1/\tau_{\rm J}^{4\pi}$. This can be straightforwardly seen in the Shapiro maps that we obtained by numerically solving the RSJ equation together with the Josephson relation $V = \frac{\hbar}{2e}\left\langle \frac{{\rm d}\phi}{{\rm d}t} \right\rangle$. In the low-frequency limit $f_{\rm rf}\tau_{\rm J}^{2\pi} < f_{\rm rf}\tau_{\rm J}^{4\pi} < 1$, all even Shapiro steps develop at rf power $P_{\rm rf}$ lower than their neighboring odd steps, leading to the following appearance sequence $|n| = \{2, 1, 4, 3, 6, 5\ldots\}$ on increasing $P_{\rm rf}$ (see Fig. 3b). Lowering $f_{\rm rf}$ would enhance this even-odd effect and result ultimately in a quasi-suppression of odd Shapiro steps. Conversely, when the drive frequency is faster than $1/\tau_{\rm J}^{4\pi}$ but still lower than $1/\tau_{\rm J}^{2\pi}$, that is, $f_{\rm rf}\tau_{\rm J}^{2\pi} < 1 < f_{\rm rf}\tau_{\rm J}^{4\pi}$, the 4π-periodic contribution is suppressed, restoring the regular sequence of Shapiro steps appearance $|n| = \{1, 2, 3, 4\ldots\}$ on increasing $P_{\rm rf}$, as shown in Fig. 3c. In a 2D space ($f_{\rm rf}$, $P_{\rm rf}$), the ranges of existence of the even and odd Shapiro steps are sketched in Fig. 3d. Importantly, the even-odd effect is robust even if $I_{\rm c}^{4\pi}$ sounds negligible compared to $I_{\rm c}^{2\pi}$, since the even-odd effect will always be present at low enough frequency as soon as $f_{\rm rf} < 1/\tau_{\rm J}^{4\pi}$. This low-frequency observability of the even-odd effect furthermore excludes an explanation for the existence 4π-periodic contribution based on Landau-Zener transitions at a soft gap, which should be otherwise enhanced at high frequencies.

Let us now consider in the same computed maps the $P_{\rm rf}$-dependence of the Shapiro steps amplitude. In contrast with the standard oscillatory behavior with a complete suppression at the resistive nodes, the even steps, including the supercurrent branch ($n = 0$), exhibit a non-vanishing amplitude at every two resistive node on increasing $P_{\rm rf}$, see Fig. 3b, c. This unusual feature has been predicted in a recent paper by Domínguez et al.[26]. It is a direct consequence of the presence of the 4π-periodic channel. It also conspicuously matches the residual supercurrent at the first node of the supercurrent branch in the experimental data of Fig. 2b, e.

We demonstrate below that the amplitude of this residual supercurrent can be quantitatively related to the 4π-periodic critical current $I_{\rm c}^{4\pi}$. Figure 4a displays the computed switching current I_0 of the Shapiro step $n = 0$, extracted from Fig. 3b as a function of $P_{\rm rf}$. This plot both highlights the oscillatory behavior of I_0 with $P_{\rm rf}$ and enables us to identify the residual supercurrent

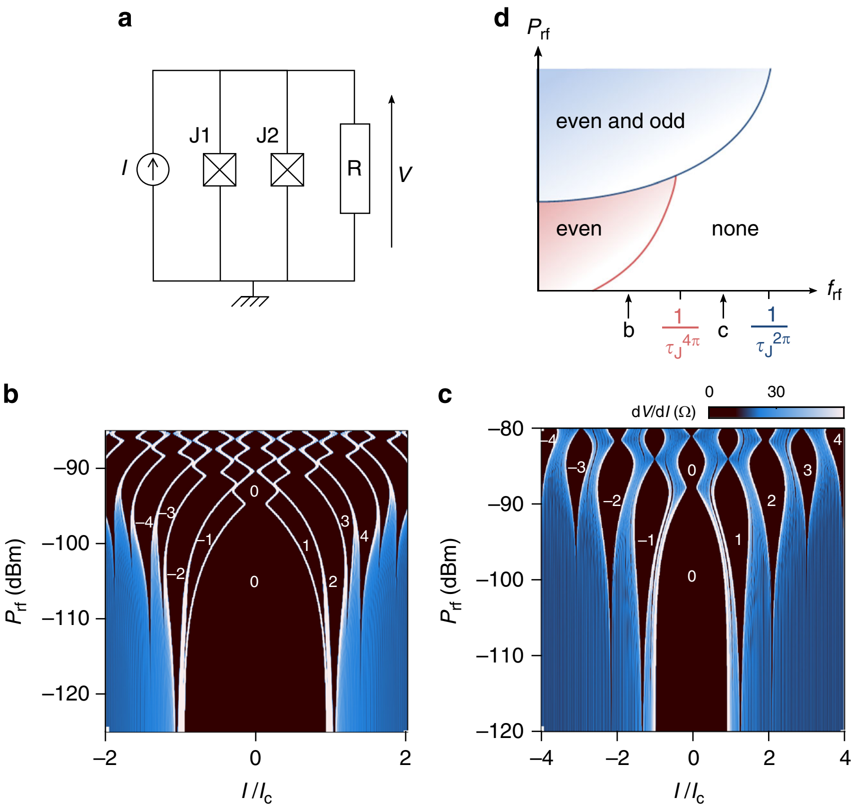

Fig. 3 Two-channel resistively shunted junction model. **a** Equivalent circuit of the two-channel resistively shunted junction (RSJ) model comprising two Josephson junctions J1 and J2 of different critical current and current-phase periodicity, that is, $I_{\rm s} = I_{\rm c}^{2\pi}\sin(\phi)$ and $I_{\rm s} = I_{\rm c}^{4\pi}\sin(\phi/2)$ respectively, in parallel with the shunt resistor R. **b**, **c** Computed Shapiro maps for the two-channel RSJ model displaying the differential resistance dV/dI versus normalized current $I/I_{\rm c}$ and $P_{\rm rf}$. The model parameters are presented in the Supplementary Note 8. The product $f_{\rm rf}\tau_{\rm J}^{4\pi} = 0.4$ and 1.5 in (**b**, **c**) respectively. **d** Range of existence of the even and odd Shapiro steps versus radio-frequency (rf) $f_{\rm rf}$ and rf power $P_{\rm rf}$. The phase relaxation times $1/\tau_{\rm J}^{2\pi}$ and $1/\tau_{\rm J}^{4\pi}$ indicate the cutoff frequency above which the contribution to the Shapiro steps of their respective channel is strongly suppressed

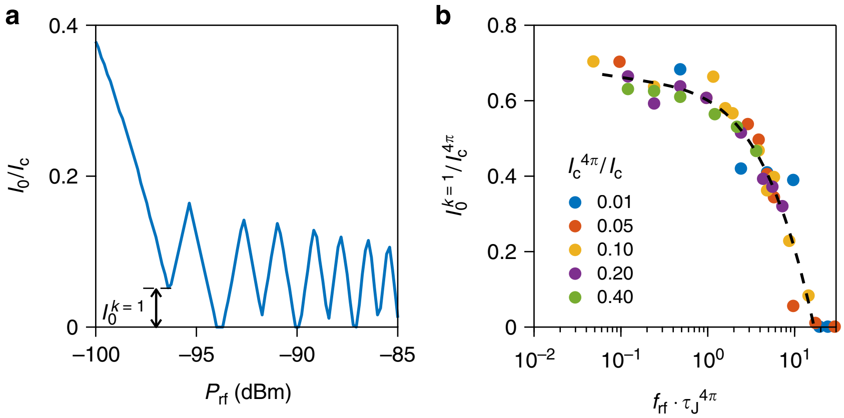

Fig. 4 Residual supercurrent. **a** Switching current of the Shapiro step $n = 0$ (supercurrent branch) I_0 normalized to the zero-power critical current $I_{\rm c}$ versus rf power $P_{\rm rf}$. I_0 is extracted from Fig. 3b. The residual supercurrent that remains at the first node $k = 1$ is noted $I_0^{k=1}$. **b** Evolution of $I_0^{k=1}$ normalized to $I_{\rm c}^{4\pi}$ versus $f_{\rm rf}\,\tau_{\rm J}^{4\pi} = f_{\rm rf}\hbar/eRI_{\rm c}^{4\pi}$ computed for various $I_{\rm c}^{4\pi}/I_{\rm c}$ ratios. All points collapse on a single curve. The black dashed line is a polynomial fit that enables to extract $I_{\rm c}^{4\pi}$ from experimental parameters. Note that fluctuations of $I_0^{k=1}/I_{\rm c}^{4\pi}$ around this dashed line stem from the limited sampling of the Shapiro maps computed

of the first node that we note $I_0^{k=1}$, with k the node index. To demonstrate the correlation between $I_0^{k=1}$ and $I_c^{4\pi}$, we performed a numerical study of the dependence of $I_0^{k=1}$ on the relevant parameters $I_c^{4\pi}$ and f_{rf} by systematically computing Shapiro maps for different sets of parameters. Figure 4b displays the calculated $I_0^{k=1}/I_c^{4\pi}$ versus $f_{rf}\,\tau_J^{4\pi}$ for different $I_c^{4\pi}/I_c$ ratios (we define here the total critical current $I_c = I_c^{2\pi} + I_c^{4\pi}$). All $I_0^{k=1}/I_c^{4\pi}$ values collapse on a single curve which tends to saturate to ~0.7 in the limit $f_{rf}\,\tau_J^{4\pi} \ll 1$. Conversely, $I_0^{k=1}$ vanishes when $f_{rf}\,\tau_J^{4\pi} \sim 16$, indicating that this residual supercurrent is visible at higher frequencies than the even-odd effect on the step appearance order.

The remarkable consequence of the collapse is that $I_c^{4\pi}$ is uniquely defined for a fixed set of parameters $I_0^{k=1}$, R and f_{rf}. Using a polynomial fit of the data points in Fig. 4b (black dashed line), we can thus directly determine $I_c^{4\pi}$ from the measured value of the residual supercurrent $I_0^{k=1}$ at a given frequency f_{rf} (see Supplementary Note 5). With the experimental parameters of Fig. 2b, that is, $R = 7.5\,\Omega$, $I_0^{k=1} = 190$ nA and $f_{rf} = 1$ GHz, we obtain $I_c^{4\pi} = 290$ nA and thus a ratio $I_c^{4\pi}/I_c \sim 4\%$. This value of $I_c^{4\pi}$ is close to the theoretical value of the supercurrent carried by a single mode $e\Delta/\hbar = 195$ nA with $\Delta = 0.8$ meV being the superconducting gap of the vanadium electrodes[46], although the exact value of the induced gap is most likely smaller than Δ due to non-perfect interface transparency. Furthermore, the resulting values $f_{rf}\,\tau_J^{4\pi} \simeq 0.3$ and 1 for the 1 and 3.5 GHz Shapiro maps of Fig. 2b and a respectively are in agreement with the presence (absence) of even-odd effect in the data, confirming the consistency of the analysis. Note that our estimate of $I_c^{4\pi}$ is close those found on strained HgTe[28] and $Bi_{1-x}Sb_x$[29] systems, which were based on the frequency cut-off criterion.

Joule-induced poisoning of the MBS. The two-channel RSJ model, however, does not account for the experimental absence of the first Shapiro step only. Inclusion of a junction capacitance geometric (or instrinsic[47]) through a two-channel RSCJ model mitigates the suppression of the $n \geq 3$ odd steps[48], but is however not relevant for our strongly overdamped Bi_2Se_3-based Josephson junctions (With a geometrical capacitance of the order of 10 aF estimated with a planar capacitor approximation for the superconducting electrodes, we obtain a damping parameter $\sigma = \sqrt{\hbar/2eI_cR^2C} \sim 260$. We also estimate an intrinsic capacitance $C^* \sim 0.1$ pF predicted in ref. [47] which leads to σ = 2.5. This overdamped regime is in contradiction with the hysteresis seen in the I-Vs, consequently bearing out the electron overheating scenario.). Furthermore, in the case of strongly underdamped, hysteresis should also be sizable in the Shapiro steps[49], which is not observed in our experiment.

We propose instead that the absence of the first step can be explained by including thermal effects resulting from Joule heating, and their impact on the 4π-periodic mode. Some of us recently showed that electron overheating must be taken into account with the RSJ model to capture Shapiro maps in conventional metallic Josephson junctions[35]. Assuming that quasiparticles in the junction form a thermal distribution with an effective temperature T_{qp} different from the phonon bath temperature T_{ph}, we included the temperature dependence of the critical current, $I_c(T_{qp})$, and solved the RSJ equation self-consistently together with the heat balance equation $P = \langle I(t)V(t)\rangle = \Sigma\Omega\left(T_{qp}^5 - T_{ph}^5\right)$ (Σ is the electron-phonon coupling constant and Ω the volume of the normal part, see Supplementary Note 6 for values) to extract T_{qp} for each dc current. Solving such a thermal RSJ model (tRSJ), we obtain a significant raise of T_{qp}, when a dc voltage drop sets in on the firstly developed Shapiro step[35].

We then conjecture that the ensuing excess of non-equilibrium quasiparticles that we express in terms of an effective quasiparticle temperature poisons the 4π-periodic mode. Note that any non-thermal distribution would have the same consequences. Acting on a single mode, poisoning causes a stochastic parity-change[15,21,22,31,44] that switches in time the quasiparticle occupation from the excited to the ground state, as illustrated in Fig. 1a by the black dotted arrow. Within the two-channel RSJ model, we model this parity-change of the 4π-periodic contribution to the supercurrent as

$$I_s^{4\pi}(t) = (-1)^{n_{sw}(t)} I_c^{4\pi} \sin\left(\frac{\phi(t)}{2}\right), \qquad (1)$$

where $n_{sw}(t)$ is a random occupation number of characteristic time scale determined by a switching parity lifetime τ_{sw} (see Supplementary Note 7). The exact microscopic processes that yield such a diabatic event can involve several transitions, including pair breaking, quasiparticle recombination with various rates, and possible coupling to the bulk states. Phenomenologically, but without loosing the generality of the foregoing, we follow the approach of Fu and Kane[15] and consider a thermally activated switching parity lifetime τ_{sw} for the 4π-periodic mode:

$$\tau_{sw} = \tau_0 \exp\left(\frac{\Delta - E_{MBS}}{k_B T_{qp}}\right), \qquad (2)$$

where $\Delta - E_{MBS}$ is the minimal energy gap separating the 4π-periodic mode to the continuum (see Fig. 1b), τ_0 the characteristic time scale for the activation process, and k_B the Boltzmann constant. When the quasiparticle effective temperature T_{qp} is high, the switching time is small $\tau_{sw} \lesssim \tau_J$ and poisoning suppresses the 4π-periodic Josephson effect, and hence the even-odd effect, by switching frequently the current-phase relation (see Supplementary Note 7). For the opposite limit $\tau_{sw} \gg \tau_J$, poisoning is irrelevant.

We thus claim that understanding the partial even-odd effect in topological Josephson junctions relies on the interplay between activated poisoning and thermal effects in the two-channel tRSJ model. We show in Fig. 5a, b two Shapiro maps computed for the same rf frequency and junction parameters as those in Fig. 3b. Figure 5a is the result of the tRSJ model that includes a T-dependence of $I_c^{2\pi}(T)$ given by the measured $I_{sw}(T)$[35] and realistic parameters for the heat balance equation (see Supplementary Note 6 for an estimate of ΣΩ in our junctions). We assume here that most of the T-dependence of $I_{sw}(T)$ comes from the 2π-periodic modes. Compared to Fig. 3b, the electron overheating leads to a broadening of the resistive transitions at high P_{rf} between the periodic oscillations of the Shapiro steps. Nevertheless, the full even-odd effect acting on all odd steps remains as in the absence of thermal effect, see Fig. 3b.

Figure 5b is the main result of our theoretical analysis. It displays a Shapiro map computed with the same tRSJ than Fig. 5a, but including thermally activated poisoning of the 4π-periodic channel defined by Eqs. (1) and (2) which ensues from Joule overheating. The 4π-periodic channel now impacts only the steps $n = \pm 2$ by enhancing their amplitude, therefore inverting the appearance order on increasing P_{rf} between step $n = 1$ and 2. The sequence of appearance of all higher order steps turns out to be regularized due to the suppression of the 4π-periodic contribution by poisoning. This finding, that is, the even-odd effect limited to the first Shapiro step only, is in full agreement with our experiment shown in Fig. 2b and with works on other systems[27–29].

The thermally activated poisoning can be captured by inspecting the computed T_{qp} and τ_{sw} for two different P_{rf}.

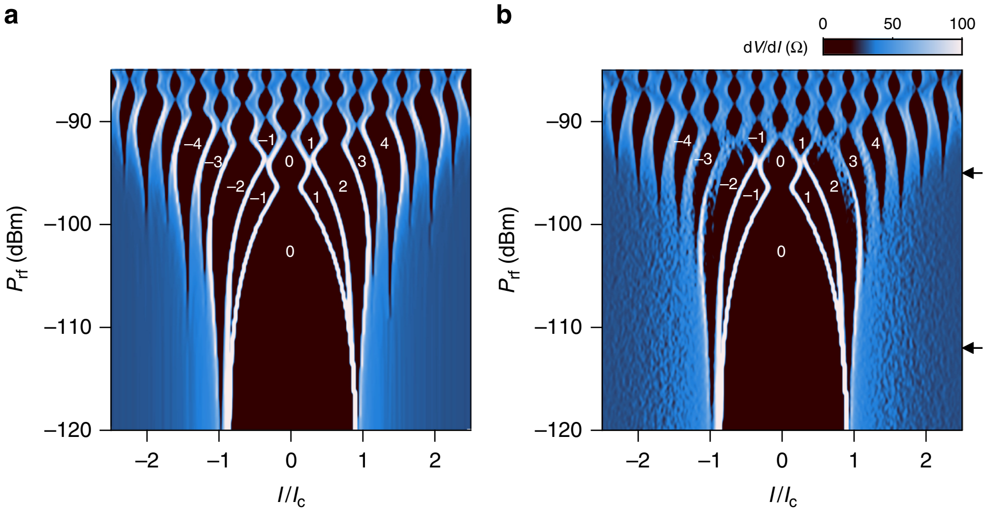

Fig. 5 Poisoning of the even-odd effect. **a** Shapiro map computed with the two-channel thermal resistively shunted junction (RSJ) model displaying the differential resistance dV/dI versus dc current I normalized to the critical current I_c and radio-frequency power P_{rf}. For the sake of clarity, we took the same parameters as in Fig. 3b, that is, $f_{rf}\tau_J^{4\pi} = 0.4$ (see Supplementary Note 8), with a phonon bath temperature $T_{ph} = 0.1$ K. The model includes the experimental T-dependence for $I_c^{2\pi}(T)$ and an estimate of the electron-phonon coupling in Bi_2Se_3 (see Supplementary Note 6). On each point a recursive algorithm solves successively the RSJ equation, the ensuing time dependent voltage and dissipated power, the raise of the quasiparticle temperature T_{qp}, and then re-solves the RSJ equation with the new $I_c^{2\pi}\left(T_{qp}\right)$ till convergence. **b** Shapiro map computed with the two-channel thermal RSJ model as in **a** but including the thermal poisoning. The implementation of a thermally activated poisoning suppresses the even-odd effect for the Shapiro step of indexes $n \geq 3$

Figure 6a displays the I-V curves corresponding to the black arrows in Fig. 5b. In Fig. 6b, we show the corresponding T_{qp} versus I, which raises linearly once a dissipative voltage sets in. Accordingly, τ_{sw} is exponentially suppressed, and becomes inferior to τ_J on the Shapiro steps $n \geq 2$ (Fig. 6c). This explains why the 4π-periodic component acts only on the appearance order of the $n = 1$ and 2 steps, leaving all other steps unaffected.

Furthermore, inspecting Fig. 5b we see that the residual supercurrent of only the first resistive node $I_0^{k=1}$ remains in presence of poisoning, as observed in the data of Fig. 2b. This confirms that the residual supercurrent $I_0^{k=1}$ is a robust feature that provides a new indicator for the presence of 4π-periodic modes, and enables a direct and quantitative determination of the corresponding 4π-periodic critical current as discussed above.

Within this approach of thermal poisoning by Joule overheating, it is interesting to compare the power dissipated between the available experiments on different TI systems. For instance, estimates of the dissipated power on the $n = 2$ Shapiro step give two orders of magnitude difference between different TI materials: $P \simeq 2\frac{hf_{rf}}{2e}I \sim 25\,\mathrm{pW}$ for our data and 17 pW for strained HgTe[28]. For InAs nanowires[27] and $Bi_{1-x}Sb_x$[29], $P \sim 2$ pW. For HgTe quantum wells[30], the dissipated power is the smallest $P \sim 0.2$ pW. Comparing the strained HgTe to the HgTe quantum wells that share the same electron-phonon coupling constant, we estimate a power per unit of volume of ~80 fW μm^{-3} and ~2 fW μm^{-3}, respectively (~300 fW μm^{-3} in our Bi_2Se_3 samples). Such a small dissipated power density in the experiment on HgTe quantum wells should result in a minimized amount of non-equilibrium quasiparticles and limited poisoning, therefore explaining the observed full suppression of not only the first but of several odd Shapiro steps in this system.

Discussion

Our theoretical approach, combining two Josephson channels in parallel, electronic overheating and quasiparticle poisoning, can be extended to more elaborate situations. For instance, recent theory works predict for the case of the quantum spin Hall regime an 8π-periodicicity due to either interactions[50] or quantum magnetic impurities[51,52]. Although this has not been reported so far in experiments, it would be interesting to study how multiple periodicities mix in the Shapiro response. Given the understanding of the two-channel RSJ model, we expect the 8π-periodicity to enhance every steps of index $\pm 4n$ and significantly modify the beating pattern at high P_{rf}. Other effects such as the voltage dependence of the phase relaxation time[21] could be included in our model and should enhance the effect of thermal poisoning on the partial suppression of the even-odd effect.

To conclude, our work elucidates the origin of the puzzling suppression of only the first Shapiro step in topological Josephson junctions. In our Bi_2Se_3 Josephson junctions, this suppression is accompanied by a residual supercurrent that provides a new indicator of the 4π-periodic contribution to the supercurrent. Together, these observations can be captured by a two-channel thermal RSJ model in which Joule overheating activates poisoning of the 4π-periodic mode. The even-odd effect restricted to the first Shapiro step and the residual supercurrent do provide a clear signature of a 4π-periodic mode in the Andreev spectrum, conspicuously pointing to MBSs. Our phenomenological model illustrates a direct consequence of thermal poisoning on MBSs, signaling that dissipation must be scrutinized with attention in dc-biased measurements. Addressing a microscopic description of the enhanced poisoning in such non-equilibrium measurement schemes is a challenging task for theory that should lead to significant progress towards new devices for Majorana physics and possible MBS qubits.

Methods

Bi_2Se_3 crystals were synthesized by melting growth method with high purity (5N) Bi and Se in an evacuated quartz tube. Crystals were analyzed by X-rays diffraction, and angle-resolved photoemission spectroscopy. Flakes of Bi_2Se_3 were exfoliated from the bulk crystal on silicon wafer and systematically inspected by atomic force microscopy to ensure crystal quality. V/Au superconducting electrodes were patterned by e-beam lithography and deposited by e-gun evaporation after a soft ion beam etching.

Measurements were performed in a dilution refrigerator equipped with highly filtered dc lines that comprise room temperature feed-through Pi-filters, lossy custom-made coaxial cables and capacitors to ground on the sample holder. Radio-

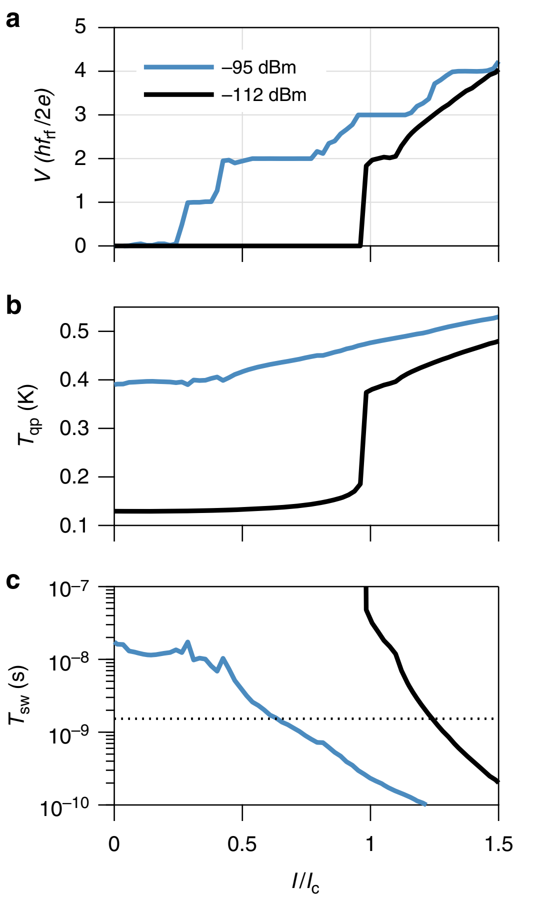

Fig. 6 Thermally suppressed parity lifetime. Data extracted from Fig. 5b at two different radio-frequency powers P_{rf} indicated by the black arrows in Fig. 5b, showing the voltage V normalized to $hf_{rf}/2e$ (**a**), Quasiparticle temperature T_{qp} (**b**), and the switching time τ_{sw} (**c**) versus current I normalized to the critical current I_c. At $P_{rf} = -112$ dBm, the first Shapiro step is absent in the $I - V$. The increase of T_{qp} when a voltage sets in on Shapiro steps leads to an exponential suppression of τ_{sw}. When $\tau_{sw} < \tau_J^{4\pi}$ (the phase relaxation time $\tau_J^{4\pi}$ is indicated by the black dotted line in **c**), poisoning suppresses the contribution of the 4π-periodic channel to the Shapiro steps $n > 2$, and all odd Shapiro steps are present in the $I - V$, see blue curve in (**a**)

frequency are fed through a dedicated coaxial cable ending as an antenna that were adjusted in the vicinity of the devices. Shapiro map measurements were performed with standard lock-in amplifier technique.

Data availability

The data that support the plots within this paper and other findings of this study are available from the corresponding author upon reasonable request.

Received: 4 June 2018 Accepted: 30 November 2018
Published online: 08 January 2019

References

1. Kitaev, A. Y. Fault-tolerant quantum computation by anyons. *Ann. Phys.* **303**, 2–30 (2003).
2. Nayak, C., Simon, S. H., Stern, A., Freedman, M. & Sarma, S. D. Non-Abelian anyons and topological quantum computation. *Rev. Mod. Phys.* **80**, 1083–1159 (2008).
3. Fu, L. & Kane, C. L. Superconducting proximity effect and majorana fermions at the surface of a topological insulator. *Phys. Rev. Lett.* **100**, 096407 (2008).
4. Mourik, V. et al. Signatures of majorana fermions in hybrid superconductor-semiconductor nanowire devices. *Science* **336**, 1003–1007 (2012).
5. Das, A. et al. Zero-bias peaks and splitting in an $Al - InAs$ nanowire topological superconductor as a signature of majorana fermions. *Nat. Phys.* **8**, 887–895 (2012).
6. Albrecht, S. M. et al. Exponential protection of zero modes in majorana islands. *Nature* **531**, 206–209 (2016).
7. Deng, M. T. et al. Majorana bound state in a coupled quantum-dot hybrid-nanowire system. *Science* **354**, 1557–1562 (2016).
8. Zhang, H. et al. Quantized majorana conductance. *Nature* **556**, 74–79 (2017).
9. Nadj-Perge, S. et al. Observation of Majorana fermions in ferromagnetic atomic chains on a superconductor. *Science* **346**, 602–607 (2014).
10. Jeon, S. et al. Distinguishing a majorana zero mode using spin-resolved measurements. *Science* **358**, 772–776 (2017).
11. Ménard, G. C. et al. Two-dimensional topological superconductivity in *Pb/Co/Si*(111). *Nat. Commun.* **8**, 2040 (2017).
12. Xu, J.-P. et al. Experimental detection of a majorana mode in the core of a magnetic vortex inside a topological insulator-superconductor $Bi_2Te_3/NbSe_2$ heterostructure. *Phys. Rev. Lett.* **114**, 017001 (2015).
13. Yu, A. Kitaev, Unpaired majorana fermions in quantum wires. *Phys.-Uspekhi* **44**, 131 (2001).
14. Kwon, H.-J., Sengupta, K. & Yakovenko, V. M. Fractional AC Josephson effect in p- and d-wave superconductors. *Eur. Phys. J. B* **37**, 349–361 (2004).
15. Fu, L. & Kane, C. L. Josephson current and noise at a superconductor/quantum-spin-hall-insulator/superconductor junction. *Phys. Rev. B* **79**, 161408 (2009).
16. Williams, J. R. et al. Unconventional josephson effect in hybrid superconductor-topological insulator devices. *Phys. Rev. Lett.* **109**, 056803 (2012).
17. Sochnikov, I. et al. Nonsinusoidal current-phase relationship in josephson junctions from the 3*D* topological insulator *HgTe*. *Phys. Rev. Lett.* **114**, 066801 (2015).
18. Kurter, C., Finck, A. D. K., Hor, Y. S. & Van Harlingen, D. J. Evidence for an anomalous current-phase relation in topological insulator josephson junctions. *Nat. Commun.* **6**, 7130 (2015).
19. Rainis, D. & Loss, D. Majorana qubit decoherence by quasiparticle poisoning. *Phys. Rev. B* **85**, 174533 (2012).
20. Albrecht, S. M. et al. Transport signatures of quasiparticle poisoning in a majorana island. *Phys. Rev. Lett.* **118**, 137701 (2017).
21. Houzet, M., Meyer, J. S., Badiane, D. M. & Glazman, L. I. Dynamics of majorana states in a topological josephson junction. *Phys. Rev. Lett.* **111**, 046401 (2013).
22. Badiane, D. M., Glazman, L. I., Houzet, M. & Meyer, J. S. AC Josephson effect in topological josephson junctions. *Comptes Rendus Phys.* **14**, 840–856 (2013).
23. Jiang, L. et al. Unconventional josephson signatures of Majorana bound states. *Phys. Rev. Lett.* **107**, 236401 (2011).
24. Domínguez, F., Hassler, F. & Platero, G. Dynamical detection of majorana fermions in current-biased nanowires. *Phys. Rev. B* **86**, 140503 (2012).
25. Virtanen, P. & Recher, P. Microwave spectroscopy of josephson junctions in topological superconductors. *Phys. Rev. B* **88**, 144507 (2013).
26. Domínguez, F. et al. Josephson junction dynamics in the presence of 2π- and 4π-periodic supercurrents. *Phys. Rev. B* **95**, 195430 (2017).
27. Rokhinson, L. P., Liu, X. & Furdyna, J. K. The fractional a.c. josephson effect in a semiconductor superconductor nanowire as a signature of majorana particles. *Nat. Phys.* **8**, 795–799 (2012).
28. Wiedenmann, J. et al. 4π -periodic josephson supercurrent in *HgTe*-based topological josephson junctions. *Nat. Commun.* **7**, 10303 (2016).
29. Li, C. et al. 4π periodic Andreev bound states in a dirac semimetal. *Nat. Mat.* **17**, 875–880 (2018).
30. Bocquillon, E. et al. Gapless Andreev bound states in the quantum spin hall insulator *HgTe*. *Nat. Nano.* **12**, 137–143 (2017).
31. Deacon, R. S. et al. Josephson radiation from gapless Andreev bound states in *HgTe*-based topological junctions. *Phys. Rev. X* **7**, 021011 (2017).
32. Sticlet, D., Sau, J. D. & Akhmerov, A. Dissipation-enabled fractional Josephson effect. *Phys. Rev. B* **98**, 125124 (2018).
33. Likharev, K. K. Superconducting weak links. *Rev. Mod. Phys.* **51**, 101–159 (1979).
34. Courtois, H., Meschke, M., Peltonen, J. T. & Pekola, J. P. Origin of hysteresis in a proximity josephson junction. *Phys. Rev. Lett.* **101**, 067002 (2008).
35. De Cecco, A., Le Calvez, K., Sacépé, B., Winkelmann, C. B. & Courtois, H. Interplay between electron overheating and AC Josephson effect. *Phys. Rev. B* **93**, 180505 (2016).
36. Sacépé, B. et al. Gate-tuned normal and superconducting transport at the surface of a topological insulator. *Nat. Commun.* **2**, 575 (2011).
37. Dubos, P. et al. Josephson critical current in a long mesoscopic $S - N - S$ junction. *Phys. Rev. B* **63**, 064502 (2001).
38. Culcer, D., Hwang, E. H., Stanescu, T. D. & Sarma, S. D. Two-dimensional surface charge transport in topological insulators. *Phys. Rev. B* **82**, 155457 (2010).

39. Dufouleur, J. et al. Enhanced mobility of spin-helical dirac fermions in disordered 3*D* topological insulators. *Nano Lett.* **16**, 6733–6737 (2016).
40. Dufouleur, J. et al. Quasiballistic transport of dirac fermions in a Bi_2Se_3 nanowire. *Phys. Rev. Lett.* **110**, 186806 (2013).
41. Hong, S. S., Zhang, Y., Cha, J. J., Qi, X.-L. & Cui, Y. One-dimensional helical transport in topological insulator nanowire interferometers. *Nano Lett.* **14**, 2815–2821 (2014).
42. Xia, Y. et al. Observation of a large-gap topological-insulator class with a single dirac cone on the surface. *Nat. Phys.* **5**, 398 (2009).
43. Snelder, M., Veldhorst, M., Golubov, A. A. & Brinkman, A. Andreev bound states and current-phase relations in three-dimensional topological insulators. *Phys. Rev. B* **87**, 104507 (2013).
44. Badiane, D. M., Houzet, M. & Meyer, J. S. Nonequilibrium josephson effect through helical edge states. *Phys. Rev. Lett.* **107**, 177002 (2011).
45. Zhang, L. et al. Ferromagnetism in vanadium-doped Bi_2Se_3 topological insulator films, APL. *Materials* **5**, 076106 (2017).
46. Beenakker, C. W. J. & van Houten, H. Josephson current through a superconducting quantum point contact shorter than the coherence length. *Phys. Rev. Lett.* **66**, 3056–3059 (1991).
47. Antonenko, D. S. & Skvortsov, M. A. Quantum decay of the supercurrent and intrinsic capacitance of josephson junctions beyond the tunnel limit. *Phys. Rev. B* **92**, 214513 (2015).
48. Picó-Cortés, J., Domínguez, F. & Platero, G. Signatures of a 4π-periodic supercurrent in the voltage response of capacitively shunted topological josephson junctions. *Phys. Rev. B* **96**, 125438 (2017).
49. Hamilton, C. A. Josephson voltage standards. *Rev. Sci. Instrum.* **71**, 3611–3623 (2000).
50. Zhang, F. & Kane, C. L. Time-reversal-invariant Z_4 fractional josephson effect. *Phys. Rev. Lett.* **113**, 036401 (2014).
51. Peng, Y., Vinkler-Aviv, Y., Brouwer, P. W., Glazman, L. I. & von Oppen, F. Parity anomaly and spin transmutation in quantum spin hall Josephson junctions. *Phys. Rev. Lett.* **117**, 267001 (2016).
52. Hui, H.-Y. & Sau, J. D. 8π-periodic dissipationless AC Josephson effect on a quantum spin hall edge via a quantum magnetic impurity. *Phys. Rev. B* **95**, 014505 (2017).

Acknowledgements
We are grateful to Manuel Houzet and Julia Meyer for inspiring comments on the poisoning processes, and Teun Klapwijk for unvaluable discussions. We thank Jacques Marcus for his support on the crystal growth. Samples were prepared at the Nanofab platform and at the “Plateforme Technologique Amont” of Grenoble. This work was supported by the LANEF framework (ANR-10-LABX-51-01) and the H2020 ERC grant *QUEST* No. 637815.

Author contributions
K.L.C. and P.P. grew the crystals. K.L.C. made the sample fabrication and carried out the measurements. F.G. provided technical support in low-temperature setups, measurements and crystal growth. K.L.C. and L.V. performed the data analysis. K.L.C. performed the numerical simulations. K.L.C., L.V., C.B.W., H.C. and B.S. discussed and interpreted the results. B.S., L.V., and H.C. wrote the paper with the inputs of all co-authors. B.S. conceived and supervised the project.

Additional information
Supplementary information accompanies this paper at https://doi.org/10.1038/s42005-018-0100-x.

Competing interests: The authors declare no competing interests.

Reprints and permission information is available online at http://npg.nature.com/reprintsandpermissions/

Publisher's note: Springer Nature remains neutral with regard to jurisdictional claims in published maps and institutional affiliations.